TIME-DEPENDENT SYNCHROTRON AND COMPTON SPECTRA FROM JETS OF MICROQUASARS

S. GUPTA AND M. BÖTTCHER

Department of Physics and Astronomy, Astrophysical Institute, Clippinger Hall 251B, Ohio University, Athens, OH 45701-2979

AND

C. D. DERMER

E. O. Hulburt Center for Space Research, Code 7653, Naval Research Laboratory, Washington, DC 20375-5352

ABSTRACT

Jet models for the high-energy emission of Galactic X-ray binary sources have regained significant interest with detailed spectral and timing studies of the X-ray emission from microquasars, the recent detection by the HESS collaboration of very high energy γ-rays from the microquasar LS 5039, and the earlier suggestion of jet models for ultraluminous X-ray sources observed in many nearby galaxies. Here we study the synchrotron and Compton signatures of time-dependent electron injection and acceleration, and adiabatic and radiative cooling in the jets of Galactic microquasars. Synchrotron, synchrotron self-Compton, and external Compton radiation processes with soft photons provided by the companion star and the accretion disk are treated. An analytical solution is introduced to the electron kinetic equation for general power-law geometries of the jets for Compton scattering in the Thomson regime. We pay particular attention to predictions concerning the rapid flux and spectral variability signatures expected in a variety of scenarios, making specific predictions concerning possible spectral hysteresis, similar to what has been observed in several TeV blazars. Such predictions should be testable with dedicated monitoring observations of Galactic microquasars and ultraluminous X-ray sources using *Chandra* and/or *XMM-Newton*.

Subject headings: gamma rays: theory — radiation mechanisms: nonthermal — stars: winds, outflows — X-rays: binaries

1. INTRODUCTION

The high-energy emission from X-ray binaries (XRBs) is generally believed to be powered by the accretion of matter from a stellar companion onto a compact object of typically a few solar masses. In many sources, this accretion process is associated with the expulsion of collimated, mildly relativistic bipolar outflows (jets) most likely perpendicular to the accretion disk. In a few sources, e.g., GRS 1915+105 (Mirabel & Rodríguez 1994), very long baseline interferometry (VLBI) radio images have shown a spatially resolved radio jet during episodes of quasi-steady and hard X-ray emission (Dhawan et al. 2000).

In the standard picture, the high-energy (X-ray–γ-ray) spectra of X-ray binaries generally consist of two major components: a soft disk blackbody with a typical temperature of $kT \sim 1$ keV, and a power law at higher energies. Neutron star and black hole X-ray binaries exhibit at least two main classes of spectral states, generally referred to as the high-soft state and the low-hard state (for a review see, e.g., Liang 1998; McClintock & Remillard 2006). The high-energy spectra of X-ray binaries in the soft state are characterized by a thermal blackbody component, believed to be associated with thermal emission from an optically thick, geometrically thin accretion disk (Shakura & Sunyaev 1973), and a power-law tail with a photon index $\Gamma \geq 2$. Generally, no high-energy cutoff of the high-energy power law is detected. In the hard state, the spectrum is dominated by a power law, with a slope $\Gamma < 2$ and a cutoff at ~few hundred keV.

In the conventional view of X-ray binaries (including microquasars), the X-ray and γ-ray emission is attributed to Comptonized emission (Sunyaev & Titarchuk 1980; Titarchuk 1994) arising from hot thermal ($kT \gg 1$ keV) or relativistic, nonthermal electrons close to the black hole (e.g., Liang & Price 1977;

Bisnovatyi-Kogan & Blinnikov 1977; Shapiro et al. 1976; Narayan & Yi 1994; Chen et al. 1995). The tentative Energetic Gamma-Ray Experiment Telescope (EGRET) detections of at least two Galactic microquasars at MeV–GeV γ-ray energies, namely, LS 5039 (Paredes et al. 2000) and LSI +61 303 (Gregory & Taylor 1978; Taylor et al. 1992; Kniffen et al. 1997); the detection of X-ray jet structures in several microquasars using *Chandra* and *XMM-Newton* (e.g., Corbel et al. 2002; Tomsick et al. 2003); and, most recently, the detection of very high energy (VHE) γ-ray emission from LS 5039 (Aharonian et al. 2005) have re-ignited interest in jet models for the high-energy emission from microquasars, analogous to the commonly favored models for blazars (for a recent review see, e.g., Böttcher 2002).

A jet origin of the X-ray emission of microquasars has previously been suggested by several authors, e.g., Markoff et al. (2001, 2003a, 2003b), who discussed the possibility of synchrotron emission from relativistic electrons in the jet extending from the radio all the way into the X-ray regime. This idea is particularly well motivated by the tight temporal correlation between the radio and hard X-ray emission in microquasars, apparently anticorrelated with the soft X-ray emission (e.g., Corbel et al. 2000, 2001).

Additional motivation for the investigation of jet models for the X-ray emission of microquasars comes from the suggestion by Georganopoulos et al. (2002) that ultraluminous X-ray sources (ULXs, with X-ray luminosities $L_X \gtrsim 10^{39}$ ergs s^{-1}), detected in many nearby galaxies (see, e.g., Makishima et al. 2000; Fabbiano et al. 2001), may be microquasars viewed at very small angles with respect to the line of sight (hence dubbed "microblazars"). However, more recent observational evidence, including indications of predominantly thermal spectra of ULXs (e.g., Miller et al. 2003) and the discovery of X-ray-ionized nebulae around

the optical counterparts of ULXs (Pakull & Mirioni 2003; Kaaret et al. 2004) provide increasing support for alternative models.

Motivated by the new observational results summarized above, various authors have been working on the expected high-energy emission signatures from microquasars. In addition to the jet-synchrotron models mentioned above, Bosch-Ramon et al. (2005a, 2005b) and Romero et al. (2005) have investigated various scenarios for the leptonic or hadronic origin of high-energy emission from microquasars, aiming in particular at explaining the potential EGRET detections of LS 5039 and LSI +61 303. Those papers concentrate on a detailed description of the high-energy emission processes in a steady state configuration. However, if leptonic emission mechanisms play a dominant role in the high-energy radiation of microquasars, then one would expect to see significant spectral variability, possibly similar to the spectral hysteresis observed in the X-ray spectra of several high-frequency peaked BL Lac objects, such as Mrk 421 (Takahashi et al. 1996) or PKS 2155−304 (Kataoka et al. 2000).

Indications of such behavior have been seen in XTE J1550−564 (Rodriguez et al. 2003), but X-ray variability correlated with flaring behaviors detected at GeV energies with the *Gamma-Ray Large Area Space Telescope* (*GLAST*) or at TeV energies with the ground-based air Cerenkov telescopes would provide strong evidence that leptonic processes are responsible for the γ-ray emission. A detailed time-dependent analysis of the high-energy emission signatures of jet models of microquasars has so far been restricted to a study of the X-ray timing signatures of an empirical power-law model for the high-energy emission (Körding & Falcke 2004), and a study of the expected quasi-periodic oscillation (QPO) features as well as broadband spectral variability correlations on longer timescales (Yuan et al. 2005). Reig et al. (2003; see also Giannios et al. 2004; Giannios 2005) proposed a model of X-ray variability from microquasar jets, in which the variability is driven by a variable soft photon source (the accretion disk), with a steady state jet configuration. Those authors focused on predictions concerning the power density spectra as well as time and phase lag features, similar to previous work for accretion disk corona models by Kazanas et al. (1997), Hua et al. (1997, 1998), Böttcher & Liang (1998), and Böttcher (2001). No predictions concerning X-ray spectral hysteresis in hardness-intensity diagram (HID) form are made.

Since it is likely that many different radiation components (synchrotron, synchrotron self-Compton [SSC], external Compton) are contributing to the high-energy emission from microquasars in the low-hard state, the rapid variability patterns expected in realistic jet models of microquasars might be more complex than the features previously investigated. In this paper, we present a detailed study of various plausible scenarios of electron injection and acceleration into a relativistically moving emission region in a microquasar jet, and subsequent adiabatic and radiative cooling. We pay particular attention to the X-ray spectral variability, as motivated above. In § 2 we present a general outline of the assumed model geometry and choice of parameters for a baseline model used for our investigation. This section also contains a brief discussion of the emission mechanisms that we include in our calculations. In § 3 we present an analytic solution to the electron kinetic equation in the case of power-law jet geometries, which is used for our time-dependent study of the radiation signatures from our model. Starting from our baseline model, we then perform a parameter study to investigate the imprint of various parameter choices on the expected spectral and var-
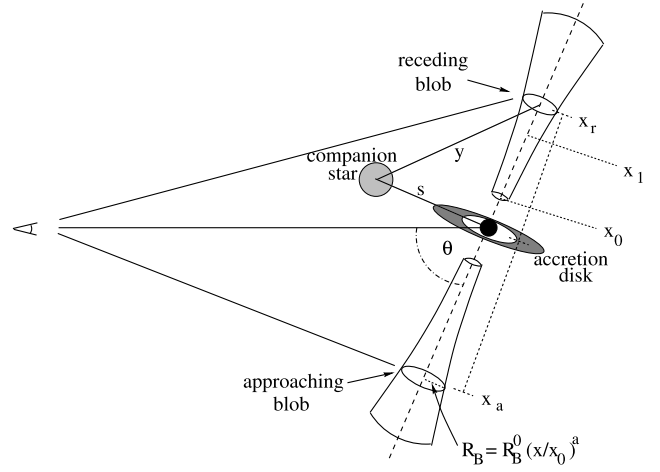

FIG. 1.—Basic geometry of our model. See text for a detailed discussion.

iability patterns from microquasars, which is presented in § 4. We summarize in § 5.

2. MODEL SETUP

The geometry of our model setup is illustrated in Figure 1. The accretion flow onto the central compact object is ejecting a twin pair of jets, directed at an angle θ with respect to the line of sight. Two intrinsically identical disturbances, containing nonthermal plasma (blobs) originate from the central source at the same time, traveling in opposite directions along the jet at a constant speed $v_j = \beta_j c$. Let d be the distance to the source, and $\mu \equiv \cos \theta$. The time at which any radio component is observed is denoted by $t_{\rm obs}$. If we wish to distinguish between the approaching and the receding blobs, we do so using the subscript a for the approaching and r for the receding component of the jet. The intrinsic times (in the stationary frame of the central source) at which those components are being observed are

$$t_{a,r}^* = \frac{t_{\rm obs}}{(1 \mp \beta_j \mu)}, \qquad (1)$$

corresponding to linear distances of $x_{a,r} = v_j t_{a,r}^*$ from the central source. Here and throughout the remainder of the paper, times t^* measured in the rest frame of the central source are denoted by the superscript *, while times t without superscript refer to the comoving frame of the blob. We assume that over a limited range in distance $x_0 \leq x \leq x_1$, relativistic electrons are accelerated and injected in the emission region. Most scenarios for the acceleration and injection of relativistic electrons in the jet will lead to a power-law spectrum of injected electrons, which we parameterize in terms of an electron injection function,

$$\frac{d^2 N_e(\gamma_i, \, t_i)}{d\gamma_i \, dt_i} = Q_0 \gamma_i^{-q} H(\gamma_i; \, \gamma_{\min}, \, \gamma_{\max}) H(t_i; \, t_0, \, t_1), \quad (2)$$

where $H(y; y_0, y_1)$ is defined as 1 for $y_0 \leq y \leq y_1$ and 0 elsewhere, and $t_{0,1} = x_{0,1}/v_j$. The normalization constant Q_0 for the electron energy distribution is related to the injection luminosity $L_{\rm inj}$ through

$$Q_0 = \begin{cases} \dfrac{L_{\rm inj}(2 - q)}{m_e c^2 \left(\gamma_{\max}^{2-q} - \gamma_{\min}^{2-q} \right)} & \text{if } q \neq 2, \\[2ex] \dfrac{L_{\rm inj}}{m_e c^2 \ln(\gamma_{\max}/\gamma_{\min})} & \text{if } q = 2. \end{cases} \qquad (3)$$

TABLE 1
PARAMETER CHOICES FOR OUR BASELINE MODEL

Parameter	Symbol	Value
Black hole mass	M	$15\ M_\odot$
Distance	d	3.75×10^{22} cm
Jet inclination angle	$\theta_{\rm jet}$	$70°$
Bulk Lorentz factor	Γ_j	2.5
Binary separation	s^*	10^{12} cm
Luminosity of companion star	L_*	8×10^{37} ergs s^{-1}
Surface temperature of the companion star	T_*	3×10^4 K
Initial blob radius	R_0	$10^3\ R_g$
Jet collimation parameter	a	0.3
Accretion fraction	$\dot{m} = \dot{M}/\dot{M}_{\rm Edd}$	0.01
Accretion disk luminosity	L_D	1.9×10^{37} ergs s^{-1}
Electron injection spectrum, low-energy cutoff	$\gamma_{\rm min}$	10
Electron injection spectrum, high-energy cutoff	$\gamma_{\rm max}$	10^4
Electron injection spectrum, spectral index	q	2.4
Beginning of electron injection zone	x_0	$10^3\ R_g$
End of electron injection zone	x_1	$10^5\ R_g$
Magnetic field at x_0	B_0	5×10^3 G
Injection luminosity	$L_{\rm inj}$	$4.4 \times 10^{-5}\ L_{\rm Edd}$

The blob's (transverse) radius, $R_\perp$, scales with distance from the central engine as $R_\perp = R_\perp^0 (x/x_0)^a$; i.e., $a = 0$ corresponds to perfect collimation, and $a = 1$ describes a conical jet. In the following, we consider values of $0 \leq a \leq 1$, and for the purpose of an analytical estimate, we assume no significant expansion along the direction of motion. Following the arguments given in Atoyan & Aharonian (1997), we choose a magnetic field dependence on distance from the central black hole as $B(x) = B_0 (R_\perp/R_\perp^0)^{-2} = B_0(x/x_0)^{-2a}$.

Each electron injected into the emission region at relativistic energies will be subject to adiabatic and radiative cooling, described by

$$-\frac{d\gamma}{dt} = \frac{1}{V_B}\frac{dV_B}{dt}\frac{\gamma}{3} + \frac{4}{3}c\sigma_{\rm T}\frac{u}{m_e c^2}\gamma^2 \qquad (4)$$

in the comoving frame of the blob, where the first term on the right-hand side describes the adiabatic losses. The second term describes synchrotron and Compton losses, with $u = u_B + u_{\rm rad}$, where $u_B = B^2/8\pi$ is the magnetic field energy density, and $u_{\rm rad}$ is the seed photon energy density for Compton scattering in the Thomson regime. The term $u_{\rm rad}$ consists of contributions from the X-ray emission from an optically thick accretion disk, from the intrinsic synchrotron radiation, and from external photons from the companion star. From the milliarcsecond resolution of the Very Long Baseline Array (VLBA) monitoring observations that have resolved superluminal-motion components in Galactic microquasars, we can estimate that such components appear on linear scales of $x \sim 10^{-3}\ x_{-3}$ pc, with $x_{-3} \sim 1$–100. The energy density of disk photons in a point-source approximation is then $u_{\rm ext} \sim 3 \times 10^{-5}\ L_{38}(x_{-3})^{-2}\ \Gamma_j^{-2}$ ergs cm^{-3}. The magnetic field energy density of $u_B \approx 4 \times 10^{-2}\ B_{\rm G}^2$ ergs cm^{-3}, where $B_{\rm G}$ is the magnetic field in Gauss. Given the estimated magnetic field values of $\sim$few tenths of Gauss estimated on scales of several mpc for GRS 1915+105 (Atoyan & Aharonian 1999), the magnetic field decay mentioned above suggests initial magnetic field values of B_0 of around several thousand Gauss at injection sites x_0 of a few thousand R_g from the black hole. Since there does not seem to be any evidence for a "Compton catastrophe" in Galactic jet sources, we may assume

that the soft photon energy density of the synchrotron radiation field is significantly lower than the magnetic field energy density. However, in high-mass X-ray binaries (HMXBs) such as Cyg X-1, LS 5039, or LS I +61°303, it is possible that the energy density in the soft photon field from the companion star is dominant over the magnetic field energy density. The soft photon energy density from a companion star of luminosity $L_* = 10^{39}\ L_{39}$ ergs s^{-1} at a separation of $s = 10^{12}\ s_{12}$ cm from the black hole primary is $u_* \approx 3 \times 10^3 (\Gamma_j^2 L_{39}/y_{12}^2)$ ergs cm^{-3}, where $y_{12} = (x_{12}^2 + s_{12}^2)^{1/2}$ is the distance between the blob and the star in units of 10^{12} cm.

The standard parameter choices for our "baseline" model are broadly representative of GRS 1915+105 in the low-hard state, which also give equipartition between the energy densities of the relativistic electrons and the magnetic field in the ejecta. Repeated Very Large Array (VLA) observations of ejection events from radio-emitting clouds of GRS 1915+105 have established that the ejecta move with a true speed of $\beta = 0.92$, giving a bulk Lorentz factor of $\Gamma_j = 2.5$, at an angle $\theta = 70°$ with respect to the line of sight (Mirabel & Rodríguez 1994). The recent measurement of rotational broadening of the early-type K giant companion star, combined with the orbital parameters, leads to a black hole mass of $14 \pm 4\ M_\odot$ (Harlaftis & Greiner 2004). For our parameter study, we have adopted a black hole mass of $15\ M_\odot$. Radial systemic velocity and radio data calculations (Fender et al. 1999; Greiner et al. 2001) have yielded a distance of $d \sim 12$ kpc to the source. Our reference values for the orbital separation of the binary and the donor star's luminosity follow from a mass function of $9.5 \pm 3\ M_\odot$ derived by Greiner et al. (2001) from infrared observations. For the disk, a mass accretion rate of 1% in Eddington units, translating to $\sim$few times $10^{-9}\ M_\odot$ yr^{-1} for a $15\ M_\odot$ black hole, is a reasonable estimate in the low-hard state (McClintock & Remillard 2006; Belloni et al. 2000). We inject electrons into the jet over a distance of about $100R_g$ and follow the evolution of the jet for about 5 days. The magnetic field values in the jet are hard to constrain, but we start at an initial value of $B_0 = 5000$ G at the base of the jet, resulting in $B \sim 0.2$–0.3 G after $\sim$4.5 days from the start of ejection (Atoyan & Aharonian 1999). The above parameter choices are summarized in Table 1.

For the purpose of an analytic treatment of the electron kinetic equation, equation (4), we rewrite it in the form

$$-\frac{d\gamma}{dt} = m\frac{\gamma}{t} + \left[\nu_0\left(\frac{t}{t_0}\right)^{-4a} + \nu_D\left(\frac{t}{t_0}\right)^{-2} + f_*(t)\right]\gamma^2, \quad (5)$$

with $m = 2a/3$,

$$\nu_0 \equiv \frac{4}{3}c\sigma_T\frac{B_0^2}{8\pi m_e c^2}, \quad (6)$$

$$\nu_D \equiv \frac{4}{3}c\sigma_T\frac{L_D}{4\pi m_e c^3\Gamma_j^2\left(1 + \beta_j\right)^2 x_0^2}, \quad (7)$$

and $f_*(t)$ is a function describing the decline of the stellar radiation field energy density with distance from the black hole. For the purpose of an analytical description, we approximate $f_*(t)$ as a broken power law,

$$f_*(t) = \frac{\xi}{x^2 + s^2} \cong \begin{cases} \xi s^{-2} & \text{for } x \le s, \\ \xi x^{-2} & \text{for } x \ge s, \end{cases} \quad (8)$$

where $\xi \cong \sigma_T L_*\Gamma_j^2/3\pi m_e c^2$. An analytic solution to equation (5) is derived in the Appendix and discussed in § 3.

Once a solution $\gamma_i(t_i; \gamma, t)$ to equation (5) is found, the electron distribution at any point in time (and thus at any point along the jet) can be calculated through the expression

$$N_e(\gamma; t) = \int_{t_0}^t dt_i \frac{d^2N_e(\gamma_i, t_i)}{d\gamma_i dt_i}\left|\frac{d\gamma_i}{d\gamma}\right|. \quad (9)$$

Additional restrictions on the integration in equation (9) and possible solutions of $\gamma(t; \gamma_i, t_i)$ are imposed by the Heaviside functions in equation (2) and are specified in § 3.

Radiation mechanisms included in our simulations are synchrotron emission; Compton upscattering of synchrotron photons, namely, SSC emission; and Compton upscattering of external photons. With the time-dependent (and thus x-dependent) nonthermal electron spectra in equation (9), we then use a δ-function approximation to estimate the νF_ν synchrotron spectral output f_ϵ^{sy} at a dimensionless photon energy $\epsilon = h\nu/m_e c^2$ (in the observer's frame),

$$F_\nu^{sy} = \frac{1}{4\pi d_L^2}\frac{h}{m_e c^2}\frac{d^2E}{dt\,d\epsilon} \quad (10)$$

and

$$\frac{d^2E}{dt\,d\epsilon} = \frac{4}{3}c\sigma_T u_B\gamma_{sy}^2 N(\gamma), \quad (11)$$

giving

$$f_\epsilon^{sy}(\epsilon, t_{obs}) = D^4\left(\frac{c\sigma_T u_B}{6\pi d^2}\right)\gamma_{sy}^3 N_e(\gamma_{sy}, t), \quad \gamma_{sy} \equiv \sqrt{\frac{\epsilon}{D\epsilon_B}}, \quad (12)$$

(Dermer et al. 1997), where $D = \left[\Gamma_j(1 - \beta_j\mu)\right]^{-1}$ is the Doppler-boosting factor; $\epsilon_B \equiv B/B_{cr}$, with $B_{cr} = m^2c^3/\hbar e = 4.414 \times 10^{13}$ G, defined as the field at which the ground-state cyclotron energy equals the rest-mass energy of the electron; t_{obs} is the

observer time, so that $t_{obs} = t/D = t_{a,r}^*/D\Gamma_j$; and E is the total synchrotron energy radiated in the system.

For the time-dependent νF_ν spectral output f_ϵ^{EC} due to Compton upscattering of external photons from the star, we use the Thomson approximation and represent the star as a monochromatic point source. We find

$$f_\epsilon^{EC}(\epsilon, t_{obs}) = D^4\left(\frac{c\sigma_T u_{ext}}{6\pi d^2}\right)\gamma_c^3 N_e(\gamma_c, t), \quad \gamma_c \equiv \sqrt{\frac{\epsilon}{D\epsilon_{ext}}}, \quad (13)$$

where u_{ext} is the Doppler-boosted seed photon energy density from the companion star (in the comoving frame), given by

$$u_{ext} = D_*^2\frac{L_*}{4\pi y^2 c}, \quad (14)$$

where ϵ_{ext} is the dimensionless photon energy due to the companion star in the comoving frame. It is related to the characteristic photon energy from the star $\epsilon_* = 2.7\,kT_*/m_e c^2$ through $\epsilon_{ext} = D_*\epsilon_*$. T_* is the effective surface temperature of the star, and $D_* = \Gamma_j(1 - \beta_\Gamma\mu_{ext}^*)$ Lorentz-transforms ϵ_* into the comoving frame.

Here we have omitted an angle-dependent factor that arises in a more accurate derivation for the spectrum of Compton-scattered stellar radiation, which is important when the orbital variability of the star is considered (Dermer & Böttcher 2006).

The photon spectrum due to Compton upscattering of photons from the accretion disk is obtained by adopting a similar formalism as that used for the companion star. We approximate the disk as a thin annulus at the radius R_{max}, where the differential energy output is maximized. We use the optically thick, geometrically thin, gas-pressure-dominated accretion disk solution of Shakura & Sunyaev (1973), predicting a blackbody spectrum according to a temperature distribution $T_D(R_{max})$ given by

$$\Theta(R_{max}) = \frac{kT_D}{m_e c^2}(R_{max}) = 1.44\left(\frac{M}{M_\odot}\right)^{-1/2}\left(\frac{\dot{M}}{M_\odot\,\text{yr}^{-1}}\right)^{1/4}$$

$$\times\left(\frac{R_{max}}{R_g}\right)^{-3/4}\left(1 - \sqrt{\frac{6R_g}{R_{max}}}\right)^{1/4}, \quad (15)$$

where R_g is the gravitational radius, $R_{max} = 9.375R_g$, T_D is the corresponding disk temperature, M is the black hole mass in units of $M_\odot$, and $\dot{M}$ is the mass accretion rate.

We also include SSC emission, keeping in mind that our analytical approach outlined in § 3 will not be applicable to situations in which the radiative output (and thus electron cooling) from SSC dominates the bolometric luminosity, since we are neglecting SSC cooling of the electrons. We use the formalism of Tavecchio et al. (1998) to calculate the SSC spectral output in the Thomson regime. In order to be able to use this formalism, we approximate our time-dependent population of relativistic electrons at any given time by a broken power-law distribution with indices n_1 and n_2 and break Lorentz factor γ_b:

$$N(\gamma) = \begin{cases} K_1\gamma^{-n_1} & \text{if } \gamma < \gamma_b, \\ K_2\gamma^{-n_2} & \text{if } \gamma_b < \gamma < \gamma_{max}, \end{cases} \quad (16)$$

where the coefficients K_1 and K_2 are related through the kinetic condition $K_1\gamma_b^{-n_1} = K_2\gamma_b^{-n_2}$. The value of γ_b is determined by the solution of the kinetic equation for electron cooling. For weakly beamed jet emission, some fraction of the radiation is expected to impinge on the cooler material in the accretion disk

and lead to fluorescent Fe Kα line emission and a reflection hump (Beloborodov 1999). The amount of radiation irradiating the disk depends on the distance between the jet emission zone and the disk, the jet inclination angle, and the bulk Lorentz factor Γ_j. X-ray emission originating at distances $\sim 10^3 R_g$ from the disk, together with $\beta_j = 0.92$ in our model, corresponds to the case of a "synchrotron-dominated jet" (Markoff & Nowak 2004; Markoff et al. 2005), where the fraction of reflected emission has been calculated to be only $\approx 1\%$–2%. We therefore do not include this component in our present calculations.

3. ANALYTIC SOLUTIONS TO THE ELECTRON KINETIC EQUATION

The dynamic equation (5) can be solved analytically for arbitrary values of a, as long as the distance dependence of the external radiation fields, characterized by $f_*(t)$, can be piecewise approximated as a power law. The solution to the electron cooling problem, as derived in the Appendix, is given by

$$\gamma(t;\ \gamma_i,\ t_i) = t^{-m}\left[\frac{1}{\gamma_i t_i^m} + \frac{\beta}{1-m-4a}\left(t^{1-m-4a} - t_i^{1-m-4a}\right) \right.$$
$$\left. + \frac{\delta}{1+m}\left(t_i^{-(1+m)} - t^{-(1+m)}\right) + \int_{t_i}^{t} f_*(t')t'^{-m}\,dt'\right]^{-1},$$
$$(17)$$

where $\beta = \nu_0 t_0^{4a}$ and $\delta = \nu_D t_0^2$. Note that one can easily incorporate as many additional external photon components with different decay slopes and normalizations as required for any specific problem at hand.

The evaluation of the time-dependent electron distribution becomes more easily tractable if we transform the t_i integration in equation (9) into an integral over the injection energy γ_i:

$$N_e(\gamma,\ t) = Q_0 \int_{\gamma_{i,\min}}^{\gamma_{i,\max}} d\gamma_i \gamma_i^{-q} \left|\frac{d\gamma_i}{d\gamma}\right|\left|\frac{dt_i}{d\gamma_i}\right|. \qquad (18)$$

The expression for the Jacobian in equation (18) based on our analytical solution is given in the Appendix (eq. [A4]). The boundaries of the integral (eq. [18]) follow from the Heaviside functions in equation (9), which also provide the relevant limits on the values of γ for which the electron distribution is nonzero. Depending on whether the emission region is currently within the zone of electron injection ($t \le t_1$) or beyond it ($t \ge t_1$), we find two sets of boundary conditions.

In the case $t \le t_1$, we have

$$\gamma_{i,\min} = \gamma$$
$$\gamma_{i,\max} = \min[\gamma_{\max},\ \gamma_i(t_0;\ \gamma,\ t)], \qquad (19)$$

with nonzero electron distribution for

$$\gamma(t;\ \gamma_{\min},\ t_0) \le \gamma \le \gamma_{\max}, \qquad (20)$$

where $\gamma_i[t_0;\ \gamma,\ t]$ is found by inversion of the solution in equation (17).

In the case $t \ge t_1$, we find

$$\gamma_{i,\min} = \max[\gamma_{\min},\ \gamma_i(t_1;\ \gamma,\ t)]$$
$$\gamma_{i,\max} = \min[\gamma_{\max},\ \gamma_i(t_0;\ \gamma,\ t)], \qquad (21)$$

with nonzero electron distribution for

$$\gamma(t;\ \gamma_{\min},\ t_0) \le \gamma \le \gamma(t;\ \gamma_{\max},\ t_1). \qquad (22)$$

The solution, equation (17), reduces to a particularly simple form in the limit of negligible radiative losses, in which the electron kinetic equation reduces to $\dot{\gamma} = -m(\gamma/t)$, and $\gamma(t;\ \gamma_i,\ t_i) = \gamma_i\,(t/t_i)^{-m}$. The local electron spectrum is then given by

$$N_e^{\mathrm{adi}}(\gamma;\ t) = Q_0 \gamma^{-q} t\,\frac{(t_{i,\max}/t)^{\eta} - (t_{i,\min}/t)^{\eta}}{\eta}, \qquad (23)$$

where $t_{i,\min}$ and $t_{i,\max}$ are determined by the Heaviside function in equation (2), and $\eta = (q-1)m + 1$. In the limit $t \gg t_1$ and $\gamma \ll \gamma_{\max}(t)$, the local electron spectrum reduces to

$$N_e^{\mathrm{adi}}(\gamma;\ t) \approx \frac{Q_0 t_1}{\eta}\gamma^{-q}\left(\frac{t}{t_1}\right)^{1-\eta}. \qquad (24)$$

4. RESULTS

A large number of simulations have been performed to study the effects of the various model parameters on the resulting broadband spectra, light curves, and X-ray HIDs. We start our parameter study with a baseline model for which we have used the standard model parameters discussed in § 2 and listed in Table 1. Subsequently, we investigate the departure from this standard setup by varying (1) the initial magnetic field B_0, (2) the luminosity of the companion star L_*, (3) the injection electron spectral index q, (4) the low-energy cutoff γ_1 of the electron injection spectrum, (5) the high-energy cutoff γ_2 of the electron injection spectrum, (6) the injection luminosity L_{inj}, and (7) the observing angle θ_{obs} and thus the Doppler-boosting factor. The parameters used for the individual runs are quoted in Table 2.

In Figure 2, we have compiled for our baseline model a sequence of comoving electron spectra (Fig. 2a), snapshot spectral energy distributions (SEDs) and the time-averaged photon spectrum (Fig. 2b), light curves at various photon energies (Fig. 2c), and a snapshot spectrum, indicating the individual emission components (Fig. 2d). Figure 2a illustrates the gradual buildup of the electron density in the emission region and their subsequent radiative and adiabatic cooling. Figure 3 illustrates the electron cooling timescales as a function of electron energy at the end of the injection period (Fig. 3a), and as a function of time for a fixed electron energy of $\gamma = 10^3$ (Fig. 3b). At the end of the injection period, the radiative cooling timescale is shorter than the elapsed time for electron energies of $\gamma \ge \gamma_b = 2.4 \times 10^3$. In our baseline model, the magnetic field energy density is higher than that of the external photon field, with

$$\frac{u_{\mathrm{ext}}}{u_B} \sim \frac{2D_*^2 L_*}{B^2 y^2 c}, \qquad (25)$$

attaining a value of 0.36 at the end of the injection period. Because of the rapid decline of the magnetic field, $B \propto x^{-2a} \propto x^{-0.6}$, the cooling timescale increases with time in our base model, as $t_{\mathrm{sy}} \propto t^{4a} \propto t^{1.2}$. For this reason, one can see a synchrotron cooling break in the electron spectra around $\gamma_b \sim 10^3$ at early times, while, at the end of the injection period, this break blends in with a gradual high-energy cutoff and is no longer

TABLE 2
PARAMETER CHOICES FOR OUR PARAMETER STUDY

Sequence	B_0 (G)	L_* (ergs s^{-1})	q	γ_1	γ_2	L_{inj} (L_{Edd})	θ_{obs} (deg)	D
1............	1.0×10^3	8×10^{37}	2.4	10	10^4	4.4×10^{-5}	70	0.583
	2.5×10^3	...	...	...	...	...	...	...
	5.0×10^3	...	...	...	...	...	...	...
	7.5×10^3	...	...	...	...	...	...	...
	1.0×10^4	...	...	...	...	...	...	...
2............	5.0×10^3	8×10^{36}	2.4	10	10^4	4.4×10^{-5}	70	0.583
	...	8×10^{37}	...	...	...	...	...	...
	...	8×10^{38}	...	...	...	...	...	...
	...	8×10^{39}	...	...	...	...	...	...
3............	5.0×10^3	8×10^{36}	1.2	10	10^4	4.4×10^{-5}	70	0.583
	...	...	1.8	...	...	...	...	...
	...	...	2.4	...	...	...	...	...
	...	...	2.8	...	...	...	...	...
4............	5.0×10^3	8×10^{36}	2.4	1	10^4	4.4×10^{-5}	70	0.583
	...	...	...	10	...	...	...	...
	...	...	...	100	...	...	...	...
	...	...	...	1000	...	...	...	...
5............	5.0×10^3	8×10^{36}	2.4	10	10^4	4.4×10^{-5}	70	0.583
	...	...	...	...	10^5	...	...	...
	...	...	...	...	10^6	...	...	...
6............	5.0×10^3	8×10^{36}	2.4	10	10^4	2.2×10^{-5}	70	0.583
	...	...	...	...	...	4.4×10^{-5}	...	...
	...	...	...	...	...	2.2×10^{-4}	...	...
	...	...	...	...	...	4.4×10^{-4}	...	...
7............	5.0×10^3	8×10^{36}	2.4	10	10^4	1×10^{35}	5	4.60
	...	...	...	...	...	...	20	2.88
	...	...	...	...	...	...	35	1.60
	...	...	...	...	...	...	70	0.583

discernible. After the end of the injection period, synchrotron cooling is initially still dominant, but adiabatic cooling is gradually taking over as the dominant energy-loss mechanism (see Fig. 3b).

The time-dependent photon spectra in Figure 2b indicate that the synchrotron and the Compton (disk) components decay even within the injection interval, due to decaying source fields. The disk photon energy density begins to decline ($\propto t^{-2}$) immediately after the onset of injection, while the stellar photon field remains basically constant for $x < s$. This manifests itself in the gradual dominance of the external Compton (EC) (star) component over the EC (disk) component in its time evolution. The EC (disk) component produces the highest energy photons, extending out to energies beyond ~ 100 GeV, but only during a very short, subsecond flash very close to x_0. If the electron injection does actually start as close to the black hole as $x_0 \sim 1000 R_g$, as we have assumed here, such high-energy radiation might suffer substantial $\gamma\gamma$ absorption in the intense radiation field of the stellar companion (Moskalenko et al. 1993; Moskalenko & Karakula 1994; Bednarek 2000; Böttcher & Dermer 2005) and might thus not be directly observable. However, as noted in the introduction, Compton scattering of the stellar radiation field or possibly also hadronic processes might very well produce VHE γ-rays at larger distances from the central compact object (Romero et al. 2003; Bosch-Ramon et al. 2005b; Dermer & Böttcher 2006), which could escape the compact radiation field of the stellar companion without significant $\gamma\gamma$ attenuation. The radio spectrum is usually flat to inverted and extends to the infrared and even beyond (Fender et al. 2000). The spectral cutoff above the GHz range in Figure 2b is a result of our choice of $\gamma_1 = 10$, the lower energy cutoff of the electron distribution. Effects of varying γ_1 are investigated in § 4.5, showing a spectral shift toward lower frequencies with lower values of γ_1. The short-time X-ray spectral variability predictions, which are the main focus of this paper, are only weakly dependent on the choice of γ_1, at least within a realistic range of $\gamma_1 \sim 1-10$. We also note (see Fig. 2d) that the contribution from the SSC photons to the total photon spectra is negligible in our base model.

Figure 2c shows light curves at different photon frequencies, one in the UV, two in X-rays, and two at γ-ray energies. From the light curves and the snapshot spectra in Fig. 2b, one can see that the synchrotron-dominated optical-UV spectra reach their maximum very rapidly and remain at an approximately constant level until the higher energy light curves reach their maxima, around the end of the injection period. The approximately constant level of the optical-UV radiation results from the opposing effects of an increasing electron density and a decreasing magnetic field. There is no significant time delay between the light-curve peaks at the various X-ray and γ-ray energies. At 24 MeV, the dip in the light curve before the end of injection is a result of the very rapid decay of the photon field density from the disk. Here, the EC (disk) component dominates very early on, but declines rapidly and becomes dominated by the rising EC (star) component within less than 1 s. In general, a rapid change in temporal slope, as seen in various light curves in Figure 2c, indicates a transition from one radiation component to another, passing through the observing range. It should be mentioned here that the hard low-frequency cutoff apparent in our photon spectra instead of a $\nu F_\nu^{sy} \propto \nu^{4/3}$ behavior at $\nu < \nu(\gamma_1)$ is a result of the δ-function approximation in our calculations.
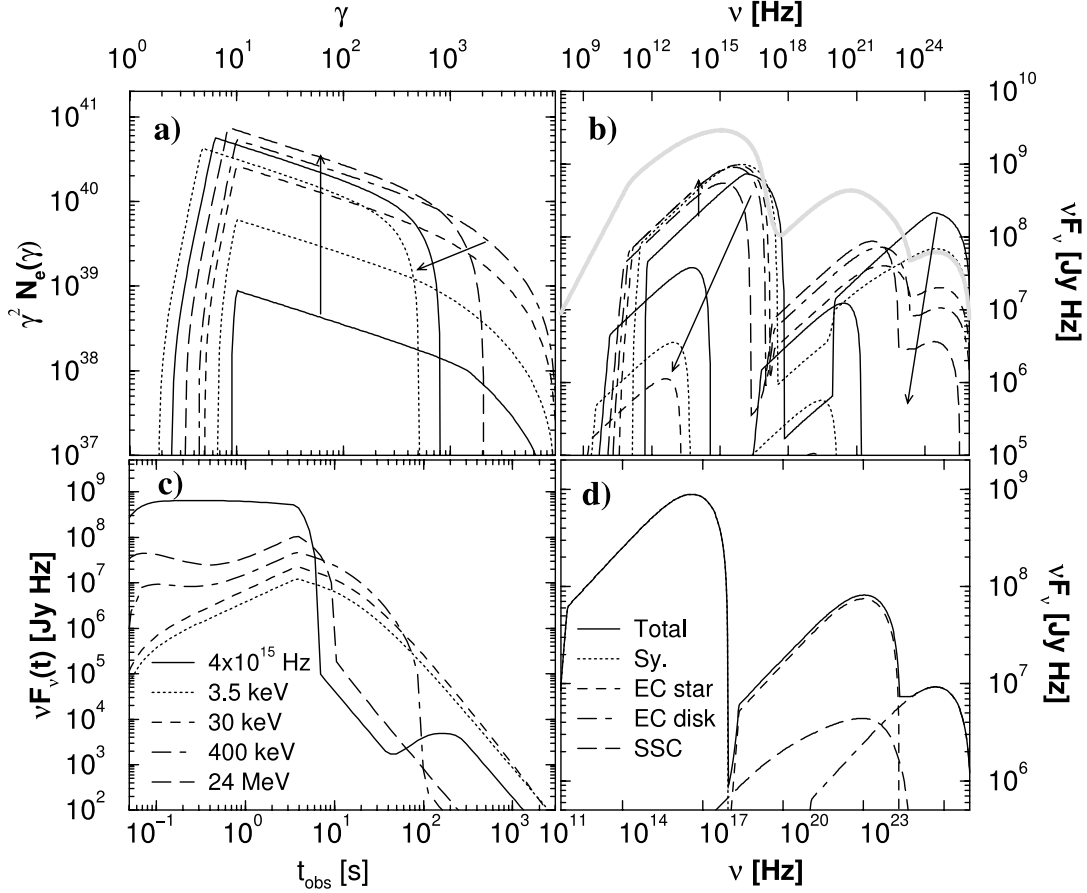
Fɪɢ. 2.—Baseline model (for parameters, see Table 1). (*a*) Time-dependent electron spectra, beginning at x_0, increasing by a multiplicative step of 10 between individual curves. The arrows indicate the sense of time evolution; the last step corresponds to a comoving time of 87.6 s. (*b*) Time-dependent νF_ν photon spectra, corresponding to the same times as shown in panel *a*. The heavy gray curve is the time-integrated flux (fluence, in units of Jy Hz s). (*c*) Light curves at five frequencies, as indicated in the key. (*d*) Snapshot spectrum just before the end of the injection period, corresponding to $t \sim 1.5$ s, showing the individual emission components.

Fɪɢ. 3.—Electron cooling timescales for our baseline model (*a*) as a function of electron energy right before the end of the injection period (same time as in Fig. 2*d*), and (*b*) as a function of time for a fixed electron energy of $\gamma = 10^3$.

In the following parameter study, we focus on the time-averaged photon spectra, light curves, and X-ray HIDs, and explore the effect of variations of individual parameters on these aspects. Throughout our study, the dominant radiative cooling mechanism will either be synchrotron or EC (star). We find that for plausible choices of parameters the contribution from SSC cooling will always be negligible, as required by our analytical approach to the solution of the electron kinetic equation given in equation (17).

4.1. Initial Magnetic Field

In this subsection, we investigate how different choices of the initial magnetic field B_0 (at x_0) influence the shape of the time-averaged photon spectra, light curves, and X-ray HIDs. The results are illustrated in Figure 4.

With increasing values of B_0, obviously the total output in synchrotron emission increases, at the expense of the Compton components. As all other parameters remain constant, this also leads to a more rapid radiative cooling of the electrons, resulting in a cooling break at lower electron energies and, consequently, lower νF_ν peak frequencies of all radiation components. Notice that the time-averaged flux at $\sim$10 keV remains almost unchanged for different magnetic field values. For the parameters adopted here, the X-ray emission is generally dominated by the EC (star) component, except for very high magnetic field values, in which case the synchrotron component initially extends into the X-ray regime. This is reflected in the very high X-ray fluxes
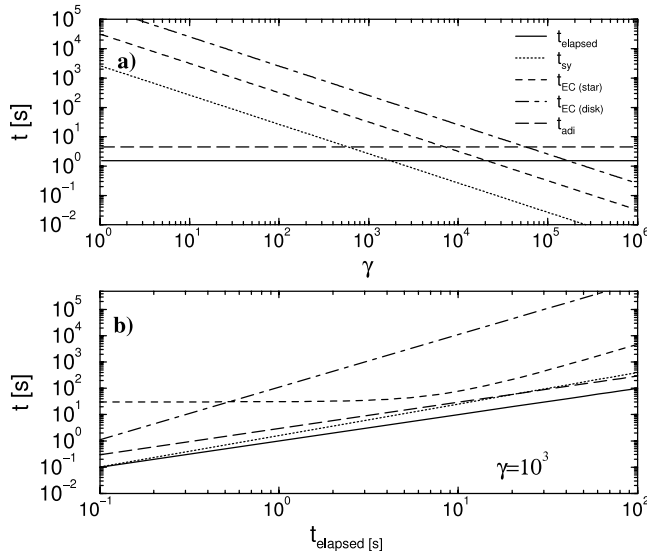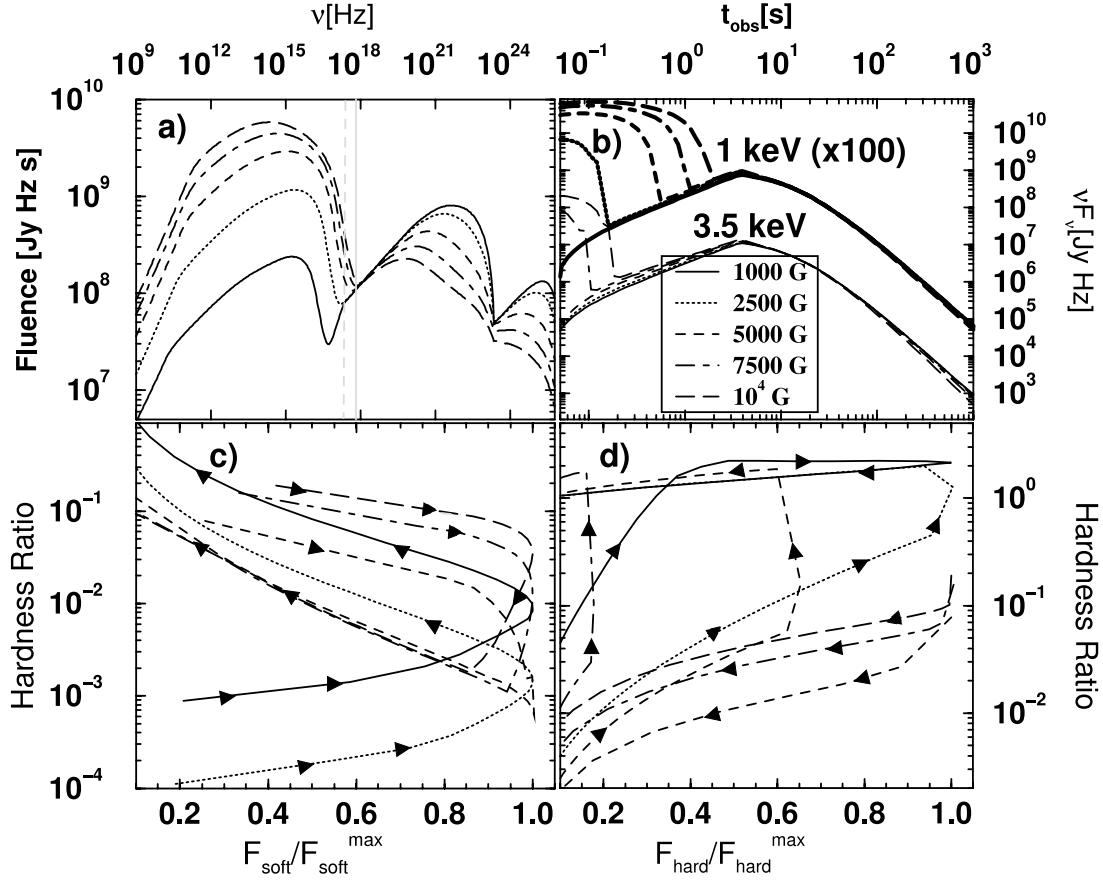
FIG. 4.—Effect of a changing magnetic field on (*a*) the time-integrated νF_ν (fluence) spectra, (*b*) the X-ray light curves at 1 keV (multiplied by 100 for clarity) and 3.5 keV, and (*c*) and (*d*) HIDs. In the HIDs, the soft flux is the integrated 0.1–2 keV flux, the hard flux is the 2–10 keV flux, and the hardness ratio is the ratio of the two. The abrupt shape of some of the HID tracks is an artifact of the δ approximations used for some of our spectral calculations. The respective magnetic fields are indicated in the key; the other parameters are the baseline model values discussed in the text and listed in Table 1. The vertical lines in panel *a* indicate the photon energies at which the light curves in panel *b* were extracted.

in the highest magnetic field cases (see Fig. 4*b*). Note that in the Compton-dominated X-ray regime (3.5 keV), the effect of different magnetic field values on the light curve is only very minor. This is because this part of the spectrum is dominated by the low-energy end of the EC (star) component, produced by low-energy electrons whose cooling is dominated by adiabatic cooling (see Fig. 3*a*), irrespective of the magnetic field.

The shorter radiative cooling timescale with increasing B_0 (and thus decreasing $\langle \gamma^2 \rangle$) also leads to an even further decreasing contribution of the SSC component, since

$$\frac{L_{\rm SSC}}{L_{\rm sy}} \sim \langle \gamma^2 \rangle \sigma_{\rm T} n_e R. \qquad (26)$$

Figures 4*c* and 4*d* compile the HIDs for the different values of B_0. Here and throughout the rest of the paper, we define the hardness ratio as the ratio of the X-ray fluxes at 2–10 keV (hard X-ray flux) to 0.1–2 keV (soft X-ray flux). The abrupt breaks in some of these tracks are an artifact of the δ approximations used in some of our spectral calculations. The HIDs trace out characteristic hysteresis loops, changing their orientation. This behavior is expected if the main contribution of the flux in a given energy bin transits between the high-energy end of one emission component to the low-energy end of another one (in this case, between the synchrotron and EC [star] components; see Böttcher & Chiang 2002). At X-ray energies around the synchrotron

cutoff, the flux maxima occur at significantly different hardness ratios for different values of B_0 (Fig. 4*d*). Specifically, within the synchrotron-dominated, clockwise spectral hysteresis loops, the peak flux is accompanied by a harder spectrum for higher magnetic fields. This is a consequence of the increasing frequency of the synchrotron peak with increasing magnetic field. Within the Compton-dominated, counterclockwise spectral hysteresis loops, the peak hard X-ray flux is accompanied by a softer hardness ratio for larger values of B_0, which is a consequence of the more efficient electron cooling.

4.2. Luminosity of the Companion Star

In our base model, as in most cases with substantial mass transfer rates onto the compact object, the external source photon field for Compton scattering is dominated by the starlight of the stellar companion. For this reason, we performed a series of simulations with increasing values of the stellar luminosity to investigate the influence of a varying external photon density on the broadband spectra, light curves, and spectral variability patterns. The results of these simulations are illustrated in Figure 5.

The time-averaged photon spectra are shown in Figure 5*a*, which clearly shows the emergence of the EC (star) component at X-ray and γ-ray energies. The impact of an increasing star luminosity on other spectral components (at radio, optical, UV, and GeV γ-rays) is small as long as the synchrotron cooling timescale is shorter than the EC (star) cooling timescale (*solid*
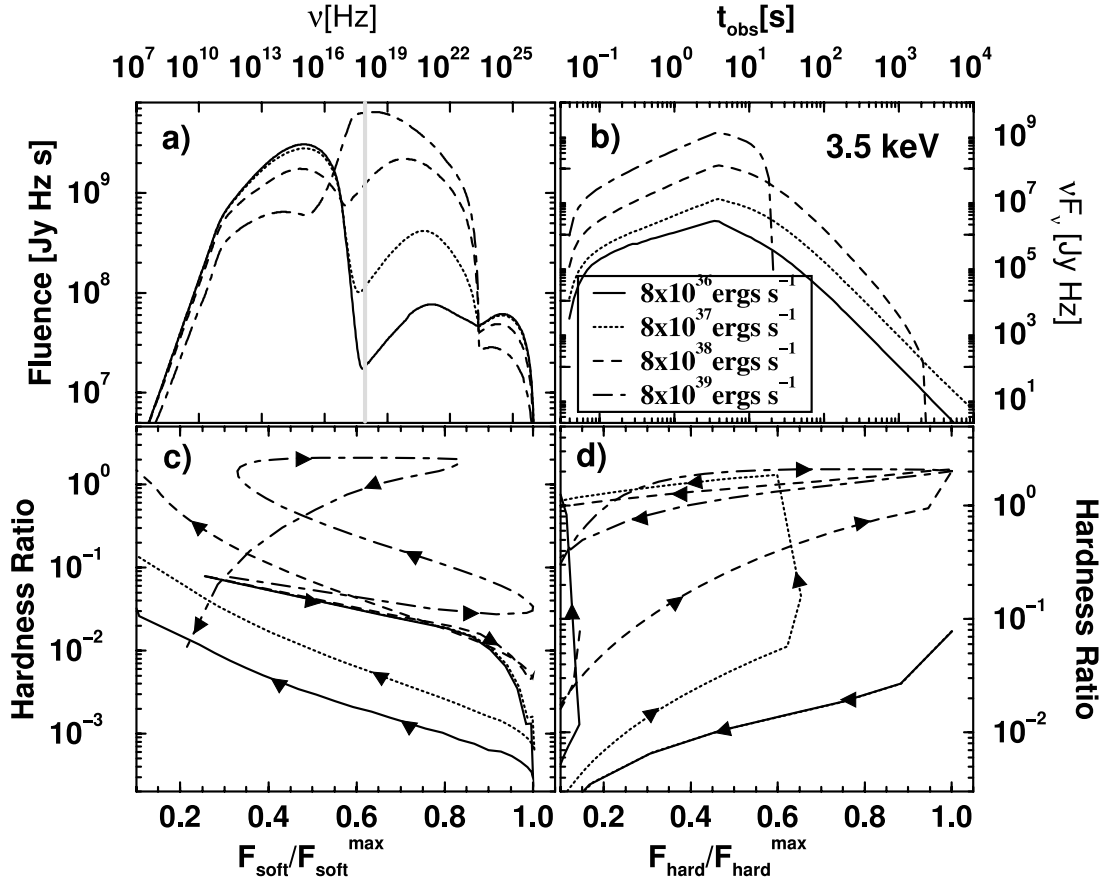
Fig. 5.—Effect of a changing luminosity of the companion star on (a) the time-integrated νF_ν (fluence) spectra, (b) the X-ray light curves at 3.5 keV, and (c) and (d) HIDs. The respective values of L_* are indicated in the key; the other parameters are the baseline model values discussed in the text and listed in Table 1. The vertical line in panel a indicates the photon energy of 3.5 keV for which the light curves in panel b are extracted.

and dotted curves). When EC cooling becomes dominant over synchrotron cooling, it leads to a reduced power output in the synchrotron and EC (disk) components as well as a shift of the νF_ν peak frequency of all radiation components toward lower values (dashed and dot-dashed curves).

Figure 5b shows that the impact of a strong EC (star) component is quite prominent in the light curve at KeV energies. Along with an increase in the peak νF_ν flux (Compton peak), an increase in the star luminosity also leads to a faster decay of the light curves in the high-luminosity cases, where the starlight radiation energy density dominates over the magnetic field energy density.

The HIDs are plotted in Figures 5c and 5d and indicate X-ray spectral hysteresis. For low values of L_*, the X-ray fluxes are initially dominated by the synchrotron flux, leading to very soft spectra at the time of the peak soft flux. As the flux decays after the end of the injection period, the EC (star) component begins to sweep through the X-ray bands, producing increasingly hard spectra during the decaying portions of the light curves (i.e., the low-flux portions of the HIDs). As L_* increases toward very high values, a secondary, counterclockwise loop in the soft-flux HID (Fig. 5c) emerges when the EC (star) component sweeps through the X-ray bands. In that case, the EC (star) component dominates the hard X-ray flux very early on, causing the overall pattern of the hard-flux HIDs (Fig. 5d) to consist only of this counterclockwise loop. We conclude that the observation of such a counterclockwise spectral hysteresis is a diagnostic of the dominance of the EC component in the X-ray regime.

4.3. Electron Injection Luminosity

The effect of an increasing injection luminosity, corresponding to a higher density of injected relativistic particles in the emitting region, is illustrated in Figure 6. This leads to a corresponding increase in the overall bolometric luminosity and a stronger energy output in the SSC component, relative to the synchrotron, as given in equation (26).

As long as the SSC emission is not dominant, this essentially only leads to a higher flux level in the spectra and light curves. At high values of L_{inj}, the SSC emission begins to play a non-negligible role in the X-ray regime, which leads to a slightly shallower slope of the X-ray light curves during the rising phase ($t < t_1$). Also, for distances $x < s$, the decay slope of the X-ray light curve is steeper for higher values of L_{inj}. Both of these effects are a consequence of the fact that the magnetic field decay is faster than that of the star photon field, and as a consequence, the decay in seed photon density for the SSC emission is faster than that for the EC (star) emission.

Figures 6c and 6d show the various HID tracks for different injection luminosities. The main effect at the soft-band HIDs (Fig. 6c) is visible in a slight hardening of the spectra during the decay phase for high values of L_{inj} as the SSC emission gradually begins to play a non-negligible role. In the hard-band HIDs (Fig. 6d), one can see that for low L_{inj}, the luminosity peak is reached very early on and is dominated by the synchrotron component leaking into the 2–10 keV band. A secondary counterclockwise loop emerges as the EC (disk) component sweeps through
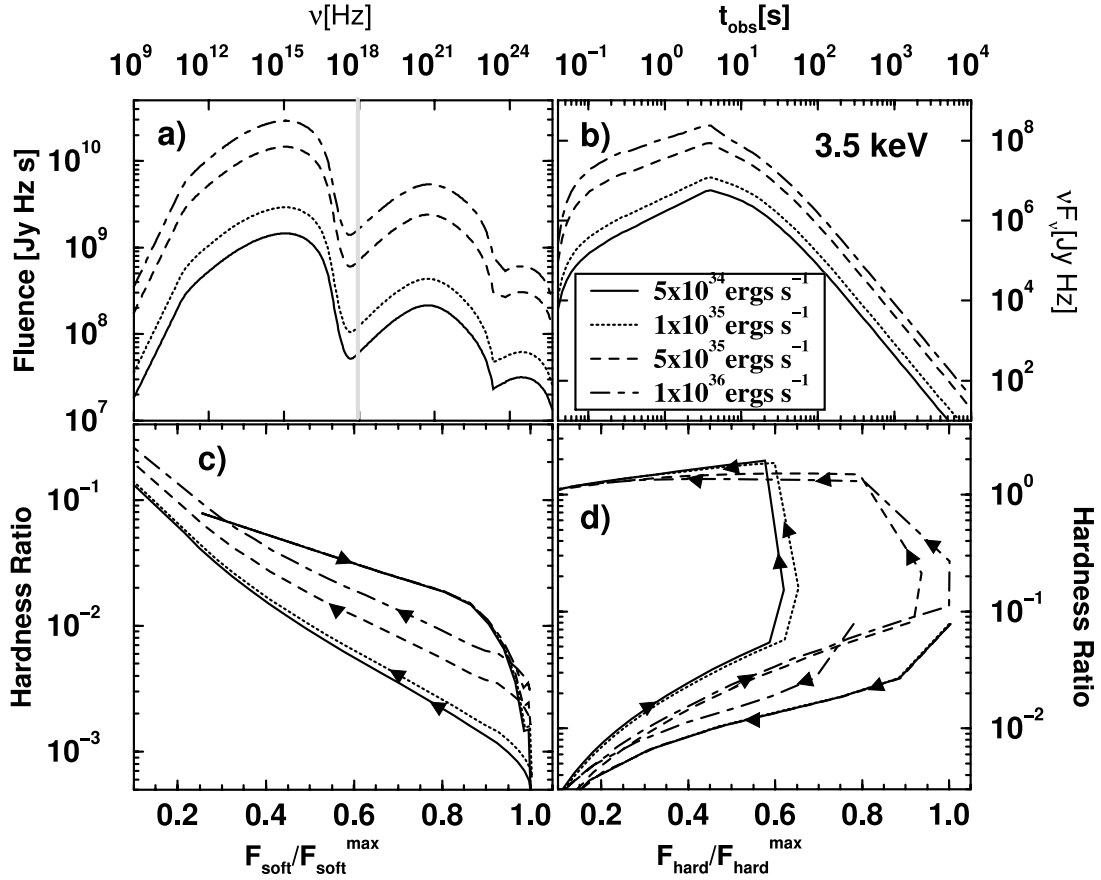
Fig. 6.—Effect of a changing electron injection luminosity (see key) on (a) the time-integrated νF_ν (fluence) spectra, (b) the X-ray light curves at 3.5 keV, and (c) and (d) HIDs. See Figs. 4 and 5 for more explanations.

the 2–10 keV band. As L_{inj} increases (along with the SSC contribution), the secondary loop extends toward higher relative flux values, until, for the highest value of L_{inj}, the peak flux occurs as the HID tracks go through the counterclockwise hysteresis loop. There is no significant difference in the local spectral index (or the hardness ratio) at the time of peak flux of the Compton-dominated hysteresis loop.

4.4. Injection Electron Spectral Index

The effect of changes in the electron injection spectral index q manifests itself obviously in the photon indices of the broadband spectra. Figure 7a shows the time-averaged photon spectra for different values of q. We see that this spectral change results in a shift of the radiation peaks toward higher frequencies as the injection spectrum hardens. We see a decreasing value of the peak flux for higher values of q (softer injection spectra) because of a decrease in the density of higher energy electrons with increasing injection spectral index. This causes a larger fraction of the injected energy to go into adiabatic rather than radiative losses (see Fig. 3a). Therefore, the jet becomes radiatively less efficient with increasing q. This also goes in tandem with a decreasing contribution from SSC, which follows directly from equation (26).

As illustrated in the light curves in Figure 7b, a higher value of q leads to a steeper decline in flux once electron injection stops. At the energy of 3.55 keV, the primary contribution is from the low-energy end of the Compton component, which is increasing with increasing spectral index. For this reason, as a higher fraction of the injected particle energy is injected near the low-

energy cutoff of the electron distribution for increasing values of q, the peak medium-energy X-ray flux during the early phase of the simulated flares is positively correlated with q. During the later decay phase, the light curves converge to rather similar shapes and flux levels, although the decay slope is still positively correlated with the spectral index, as expected.

The X-ray spectral hysteresis at energies just below and above the synchrotron cutoff is shifted according to the change in electron injection spectral index, but the overall characteristics remain unchanged (see Fig. 7c). The peak flux is reached at a higher value of the hardness ratio for a softer injection spectrum. The hardness ratio decreases during the rising portion of the soft X-ray flux light curve and increases during the decaying phase as the synchrotron component transits through the soft X-ray bands and gives way to an increasing contribution of the Compton components. The hard X-ray flux is initially also dominated by synchrotron emission, except in the case of the softest injection index, $q = 2.8$. As the synchrotron component rapidly moves out of the hard X-ray band, accompanied by a decreasing hardness ratio, the Compton component becomes dominant, and a secondary, counterclockwise hysteresis loop develops in the cases of soft electron injection spectra.

4.5. Low-energy Cutoff of the Electron Spectrum

Since we have parameterized our injection spectra through an injection luminosity, and the bulk of the kinetic energy of electrons in the jet is carried by the lowest energy electrons for spectral indices of $q > 2$, a change of the low-energy cutoff of the electron spectrum, γ_1, naturally has quite dramatic effects on the
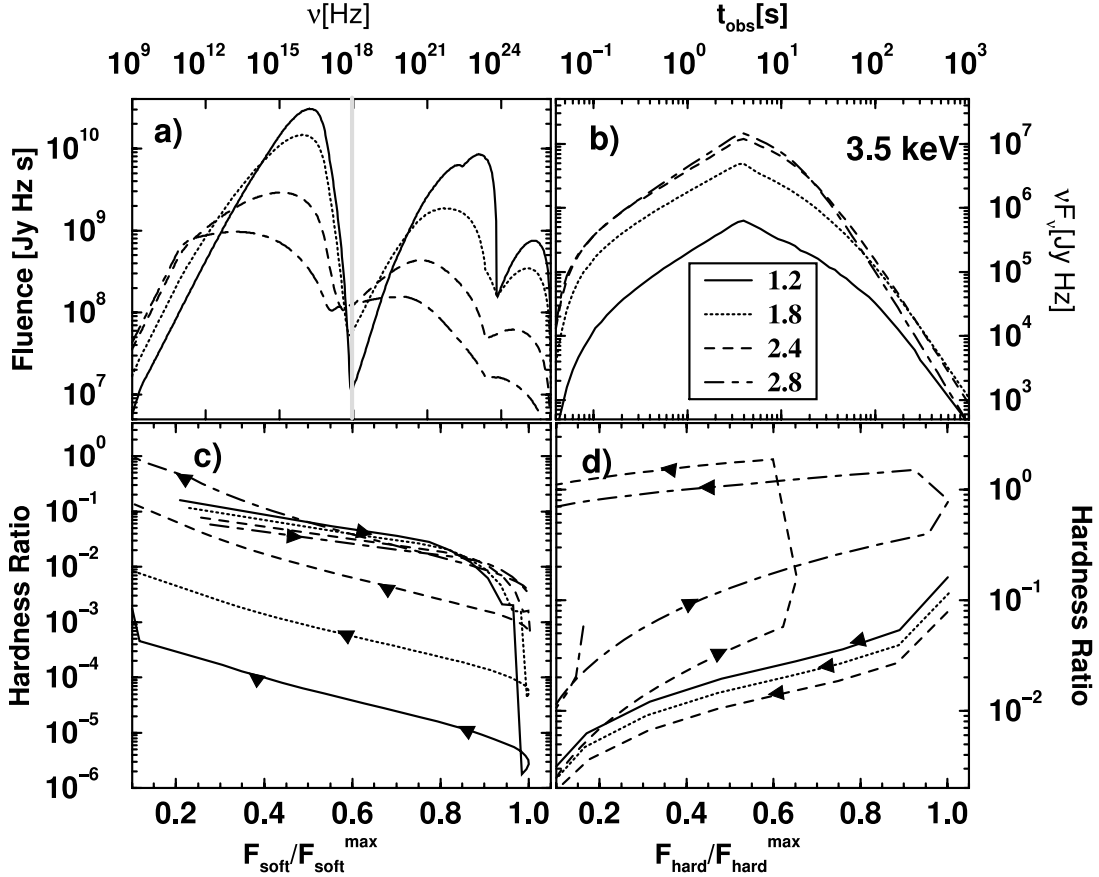
Fig. 7.—Effect of a changing electron injection spectral index (see key) on (*a*) the time-integrated νF_ν (fluence) spectra, (*b*) the X-ray light curves at 3.5 keV, and (*c*) and (*d*) HIDs. See Figs. 4 and 5 for more explanations.

radiative signatures from microquasar jets. These are illustrated in Figure 8. Because of the dominance of adiabatic losses at low electron energies, the jet becomes radiatively more efficient for higher values of γ_1. Consequently, the total radiative energy (fluence) increases, as also seen in § 4.4 as a consequence of a harder electron injection spectrum. This also goes in tandem with an increased contribution of SSC to the high-energy emission. A higher value of γ_1 shifts the low-frequency cutoff of the individual radiation components toward higher frequencies. However, since the νF_ν peak frequency is dominated by emission from the highest energy electrons for $q < 3$ (in the slow-cooling regime), a change of the value of γ_1 does not affect the νF_ν peak frequency of the individual radiation components. The shift of the high-energy peak into the γ-ray regime for $\gamma_1 = 10^3$, as seen in Figure 8*a*, is a consequence of the SSC component becoming dominant over the EC (star) component compared to the lower values of γ_1.

The increasing contribution from SSC for $\gamma_1 = 10^2$ and 10^3 is also reflected in the light curves plotted in Figure 8*b*. It is evidenced in the faster onset, but then the flatter rising portion of the flux for $\gamma_1 = 10^2$ and the faster initial decay of that light curve, until the EC (star) component begins to move through the observing frequency (3.55 keV), resulting in a similar decay as in the lower γ_1 cases. In the case of $\gamma_1 = 10^3$, the SSC component always dominates the 3.55 keV X-ray light curve.

The HIDs shown in Figures 8*c* and 8*d* confirm these findings: in the synchrotron-dominated portions of the X-ray flux (soft X-rays), the spectral hysteresis loops are clockwise and rather similar; however, for higher values of γ_1, the hardness ratio becomes significantly lower because of the increasing low-energy

cutoff of the Compton spectra. The HIDs for the hard X-ray flux show a trend similar to that described in § 4.4; in particular, for low or moderate values of γ_1, a spectral softening during the early flux decay is followed by a counterclockwise secondary hysteresis loop due to the influence of the EC (star) component.

4.6. *High-energy Cutoff of the Electron Spectrum*

A higher cutoff of the electron injection spectrum will manifest itself in the broadband spectra primarily by the extension of all radiation components toward higher energies, as can be seen in Figure 9*a*. Since only a minor portion of the overall particle energy is carried by the highest energy particles, the overall energetics of the particle distribution and the bolometric luminosity and radiative energy output of the emission region and the individual radiation components remain virtually unchanged. For high values of γ_2, the individual radiation components are increasingly overlapping, leading to a much smoother overall shape of the broadband spectrum.

The 3.55 keV light curves plotted in Figure 9*b* clearly show the marked difference between the case of relatively low γ_2, where the influence of the synchrotron component at 3.55 keV is very minor, and the high-γ_2 cases, where the synchrotron component extends significantly beyond that energy. For our standard choice of $B_0 = 5$ kG and D $= 0.583$, the critical electron Lorentz factor for synchrotron emission at 3.55 keV is $\gamma_{sy,0} = 10^4$, while at the end of injection this value has increased to $\gamma_{sy,1} = 4 \times 10^4$ due to the corresponding decline of the magnetic field over the injection length. The (comoving) synchrotron cooling timescale for electrons emitting 3.55 keV synchrotron radiation at the end of the injection period is $t_{sy} = 0.2$ s.
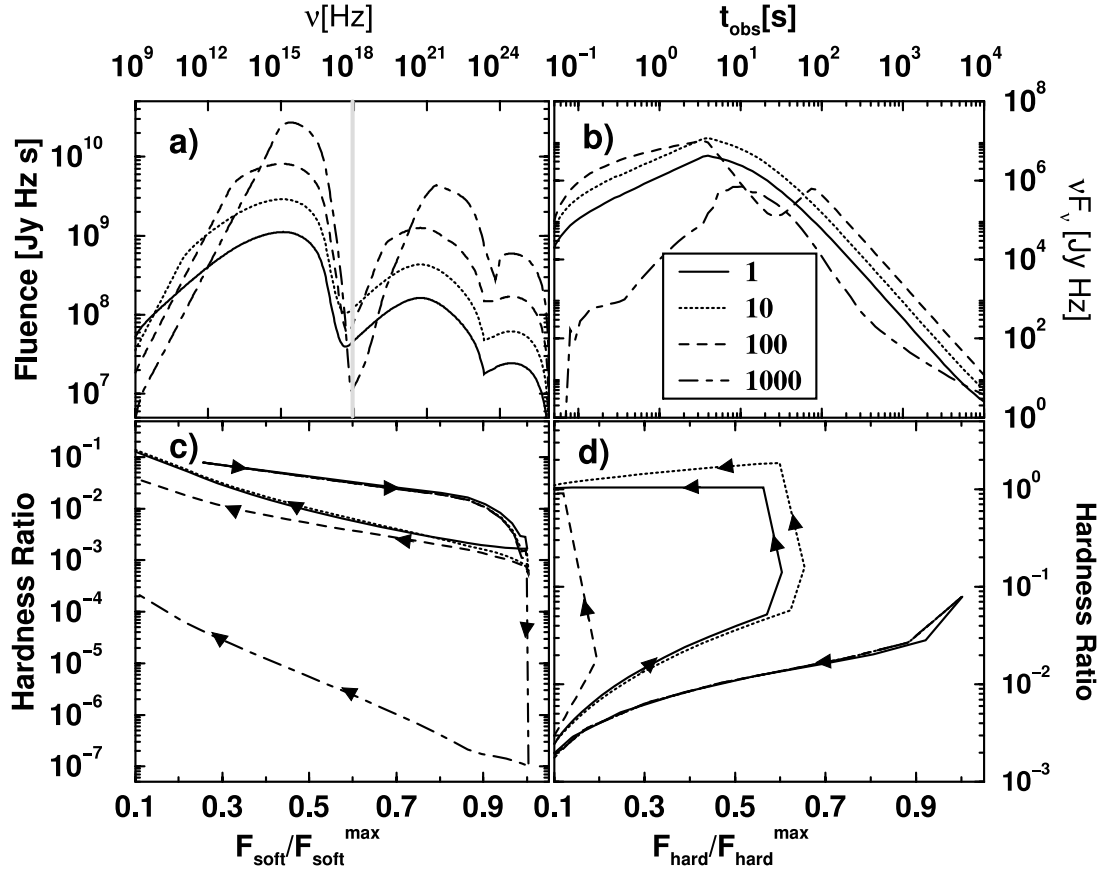
FIG. 8.—Effect of a changing low-energy cutoff of the electron distribution, γ_1 (see key), on (*a*) the time-integrated νF_ν (fluence) spectra, (*b*) the X-ray light curves at 3.5 keV, and (*c*) and (*d*) HIDs. See Figs. 4 and 5 for more explanations.
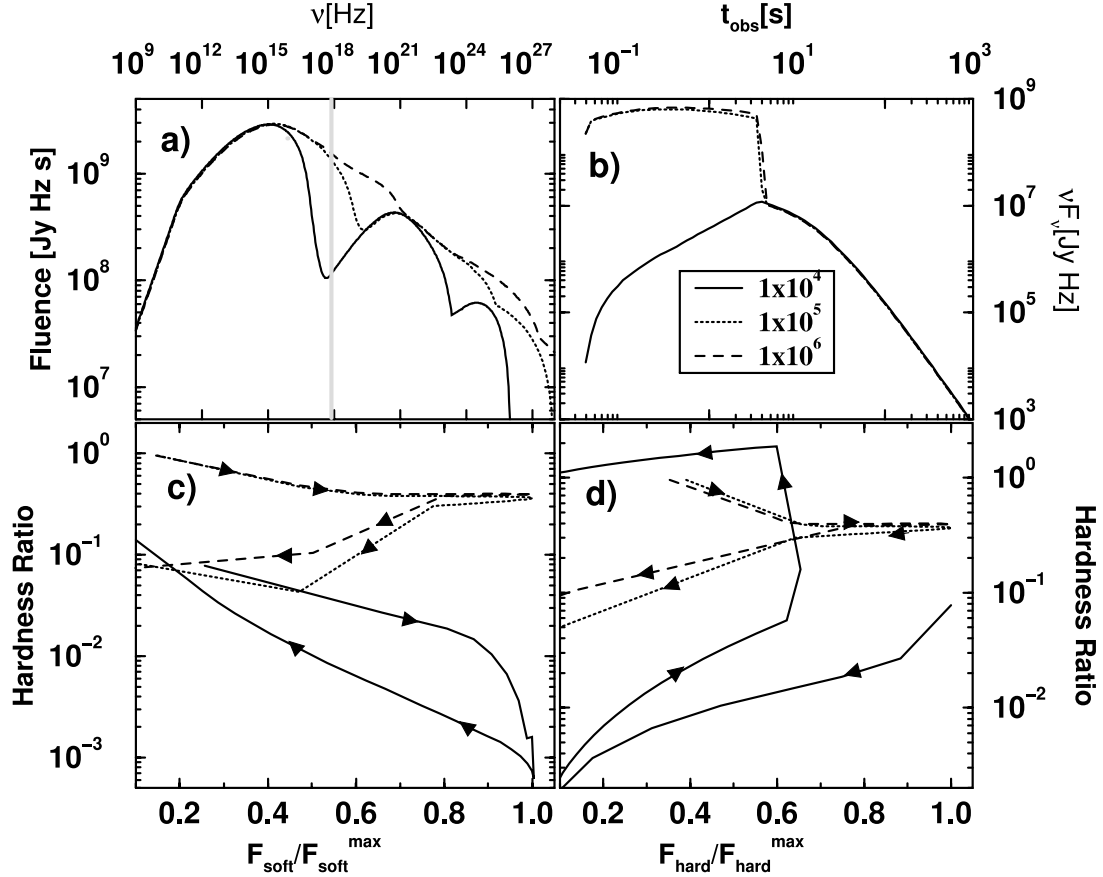

FIG. 9.—Effect of a changing high-energy cutoff of the electron distribution, γ_2 (see key), on (*a*) the time-integrated νF_ν (fluence) spectra, (*b*) the X-ray light curves at 3.5 keV, and (*c*) and (*d*) HIDs. See Figs. 4 and 5 for more explanations.
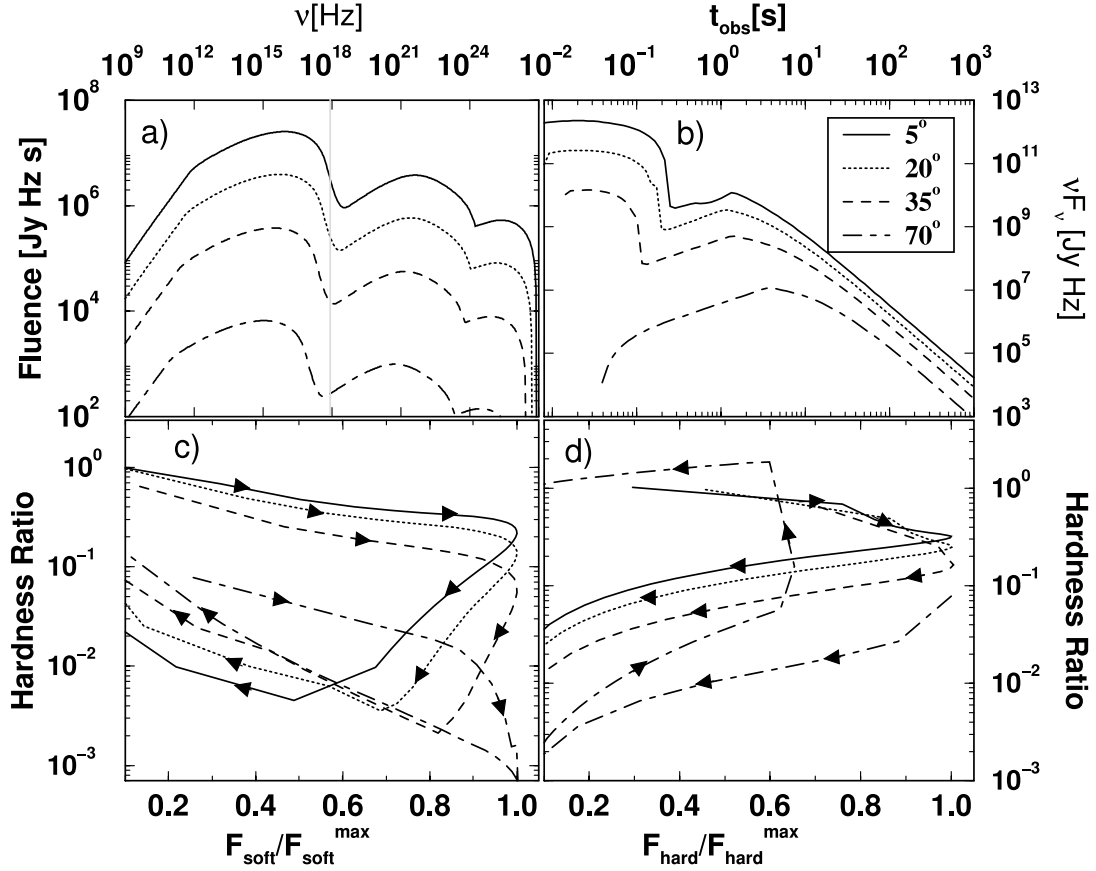
Fig. 10.—Effect of a changing viewing angle (see key) and thus of the Doppler-boosting factor, on (*a*) the time-integrated νF_ν (fluence) spectra, (*b*) the X-ray light curves at 3.5 keV, and (*c*) and (*d*) HIDs. See Figs. 4 and 5 for more explanations. The values of the Doppler factor D corresponding to the various inclination angles are $D(5°) = 4.60$, $D(20°) = 2.88$, $D(35°) = 1.60$, and $D(70°) = 0.583$.

Consequently, the synchrotron contribution to the 3.55 keV light curve disappears virtually instantaneously after the end of injection, so that the three light curves are basically identical beyond that point.

Figure 9*c* reflects the fact that during the rising phase of the light curve, the soft X-ray flux is clearly dominated by synchrotron emission. In the high-γ_2 cases, the synchrotron cutoff is located beyond the soft X-ray regime, leading to a relatively hard soft X-ray spectrum that gradually softens due to the development of a cooling break moving through the 0.1–2 keV flux. For $\gamma_2 = 10^4$, the effect of radiative cooling is immediately visible even in the soft X-ray regime, leading to a systematically softer hardness ratio near the time of soft X-ray peak flux. The secondary hard X-ray spectral hysteresis visible in the $\gamma_2 = 10^4$ case is not evident in the higher γ_2 cases only because of the much higher peak flux, so those hysteresis loops occur at much lower relative flux values (compared to the maximum flux).

4.7. *Doppler-boosting Factor*

We have investigated the effect of changing the Doppler factor D on the spectra, light curves and HIDs by changing the observing angle θ_{obs}. Figure 10*a* illustrates the spectral change resulting from a varying observing angle, given essentially by $\nu_{obs} \propto D$ and $\nu F_\nu \propto D^4$ for intrinsically isotropic emission (note, however, that the dependence is somewhat stronger for EC emission; e.g., Dermer 1995).

The 3.55 keV light curve (Fig. 10*b*) and HIDs (Figs. 10*c* and 10*d*) illustrate the gradual shift of the synchrotron emission out of the X-ray regime for lower Doppler factors (between indi-

vidual runs), and a decaying magnetic field as well as the development of the cooling break, moving through the X-ray energy range (within individual runs). In particular, this leads to synchrotron-dominated clockwise spectral hysteresis loops in the soft X-ray HIDs, and the emergence of secondary, EC (star) dominated, counterclockwise hysteresis loops in the hard X-ray HIDs for lower beaming factors. At times when the synchrotron component no longer has any influence on the X-ray light curves, the X-ray emission at 3.55 keV is dominated by the EC (star) component, and we observe two separate regimes, depending on the Doppler factor. For smaller Doppler-boosting factors, the spectral break corresponding to starlight scattered by electrons that were injected at $\gamma = \gamma_1$ occurs always below 3.55 keV. In that case, the peak in the X-ray light curve corresponds to the end of electron injection at $t_{b,obs} = t_1/D$. Consequently, it shows up at earlier observed times for increasing values of D. For higher values of the beaming factor, initially the observing frequency is below the break frequency corresponding to γ_1. In that case, the X-ray light curve keeps rising even after the end of the injection period, and the peak corresponds to the time when the break frequency becomes lower than the observing frequency. Since this happens well after the end of electron injection, the time of peak flux in this case is in fact later than that for smaller beaming factors, which explains the later light-curve peak for $\theta = 5°$ compared to $\theta = 20°$. Since the cooling of electrons injected at $\gamma_1 \lesssim 100$ is dominated by adiabatic losses, their energy decreases as $\gamma(t) \propto t^{-m}$. Consequently, we expect a dependence $t_{b,obs} \propto D^{-0.3/a}$ once the transition to this regime has occurred.

5. SUMMARY AND CONCLUSIONS

We have presented a detailed parameter study of the spectra resulting from time-dependent injection and acceleration, and adiabatic and radiative cooling of nonthermal electrons in the jets of Galactic microquasars. Jet models of microquasars have recently attracted great interest, especially after the detection of VHE γ-ray emission from the high-mass X-ray binary and microquasar LS 5039, in combination with the tentative identification of several microquasars with unidentified EGRET sources. These detections have confirmed the idea that microquasars are a distinctive class of high- and very high energy γ-ray sources.

It remains an open question whether the high-energy emission from microquasars is associated with leptonic or hadronic primaries. Predictions for the correlated variability at X-ray and high-energy γ-ray energies provide a discriminant between the two possibilities. As shown here, X-ray hysteresis diagrams are predicted in nonthermal leptonic models of microquasars, similar to the situation for blazars. Detection of such variability behavior, particularly if correlated with γ-ray flaring behavior as described here, would provide evidence in favor of leptonic models.

Whereas previous studies have largely focused on spectral fits to the broadband emission of microquasars in a steady state approximation, we have focused on the spectral variability features expected in generic microquasar jet models with electron injection and/or acceleration over a limited amount of time and length along the jet, representative of, e.g., internal shock models. We have conducted a detailed parameter study, investigating the impact of variations of several fundamental model parameters on the broadband SEDs, X-ray light curves, and the rapid X-ray spectral hysteresis phenomena expected to arise in these scenarios. We have provided an analytical solution to the electron kinetic equation, taking into account radiation signatures of synchrotron, external Compton (with seed photons from the companion star and the accretion disk), as well as synchrotron self-Compton emission. In order to be able to work with an analytical solution to the electron kinetic equation, we restricted our analysis to Compton scattering in the Thomson regime. Consequently, our results are important to derive diagnostics of microquasar jet emission in the X-ray regime and to contrast predictions of thermal Comptonization models of these sources, but are primarily applicable to microquasars that are not candidates of VHE γ-ray emission. We have neglected the angle dependence of the stellar radiation field (Böttcher & Dermer 2005; Dermer & Böttcher 2006), which would lead to a modulation of the $\gamma\gamma$ absorption trough as well as the Compton-scattered stellar radiation spectra depending on the orbital phase ($\phi_0 = 0$ showing the most absorption but highest Compton flux). The spectrum is expected to be further modified by pair cascades, redistributing some of the VHE radiative power to lower frequencies and significantly increasing the transparency of the source (Aharonian et al. 2005). A study incorporating full Klein-Nishina effects on Compton scattering, the angle dependence of the stellar radiation field, and cascade processes will be presented in a forthcoming publication on this subject.

Obviously, various spectral components (synchrotron, SSC, external Compton) could be easily distinguished if detailed snapshot SEDs could be measured for microquasars, on the (often subsecond) timescales of their X-ray variability. Unfortunately, such detailed snapshot broadband spectra are currently not available and might not be available in the near future. Therefore, we have exposed several other features pertinent to the transition between different spectral components that will be more easily observable in realistic observational data of microquasars:

1. A sudden increase of a light-curve slope at a fixed observing frequency, not accompanied by significant flaring activity at other wavelengths, usually indicates the passing of a new spectral component through the fixed observing frequency range. Most notably, this diagnostic can be used to investigate the presence of one or more external Compton component(s) in the X-ray / soft γ-ray regime.

2. Clockwise spectral hysteresis in the hardness-intensity diagrams indicates the dominance of synchrotron emission (in particular, before the end of the injection period in our generic model setup). In this case, the frequency-dependent light-curve decay will be a useful diagnostic of the magnetic field strength in the jet (e.g., Takahashi et al. 1996).

3. Counterclockwise spectral hysteresis in the hardness-intensity diagrams indicates the dominance of Compton emission (similar to the case of blazars; see, e.g., Böttcher & Chiang 2002).

4. In our study, we find, quite often, a coexistence of clockwise and counterclockwise X-ray hysteresis loops, which would provide a particularly powerful diagnostic, as it would allow us to probe the characteristic transition energy between synchrotron and Compton emission, and its time dependence.

There are only very few papers that present X-ray variability in the form of HIDs. Those papers presented long-term variability information from *Rossi X-Ray Timing Explorer* (*RXTE*) Proportional Counter Array (PCA) observations, spanning timescales of hundreds of days, thus representing the spectral characteristics of state transitions rather than the short-term variability patterns that are the focus of our analysis (see, e.g., Fender et al. 2004; Belloni et al. 2005). In such a representation, possible hysteresis on short (intraday) timescales are very hard to identify. An example in which such short-term spectral hysteresis may be identified can be found at Open Source,[1] which shows an HID for GRO 1655−40. Here, within the overall long-term variability pattern, individual short flares (over a few days) can be discerned. One such outburst around MJD 53,600 shows a spectral hysteresis, which when transformed to the orientation of the axes of HIDs in this paper, results in a counterclockwise loop, indicating Compton-dominated emission from the outflow for this outburst.

We conclude therefore that the X-ray variability as predicted by our model can be used as a diagnostic to gain insight into the nature of the high-energy emission in microquasar jets. In particular, a transition between clockwise and counterclockwise spectral hysteresis would allow not only the distinction between different emission components, but also parameters such as the magnetic field, the Doppler-boosting factor, and the characteristic electron injection/acceleration time.

---

[1] See http://tahti.mit.edu/opensource/1655/.

APPENDIX A

ANALYTIC SOLUTION OF THE ELECTRON KINETIC EQUATION

The general electron cooling equation (5) can be solved analytically by virtue of the substitution

$$y = \gamma t^m, \tag{A1}$$

which reduces equation (5) to

$$-\frac{dy}{dt} = \left[\beta t^{-4a} + \delta t^{-2} + f_*(t) \right] t^{-m} y^2, \tag{A2}$$

with β and δ defined after equation (17). This can easily be integrated to give

$$\frac{1}{y} - \frac{1}{y_i} = \frac{\beta}{1-m-4a} \left(t^{1-m-4a} - t_i^{1-m-4a} \right) - \frac{\delta}{1+m} \left(t^{-(1+m)} - t_i^{-(1+m)} \right) + \int_{t_i}^{t} f_*(t') t'^{-m} \, dt'. \tag{A3}$$

Substituting $y = \gamma t^m$ yields the solution (eq. [17]) in the main text.

The Jacobian in equation (18) is

$$\left| \frac{d\gamma_i}{d\gamma} \right| \left| \frac{dt_i}{d\gamma_i} \right| = \left(\frac{t_i}{t} \right)^m \frac{\gamma^{-2}}{m/\gamma_i t_i + \beta/t_i^{4a} + \delta/t_i^2 + f_*(0)}, \tag{A4}$$

resulting in an electron spectrum at any given point along the jet:

$$N_e(\gamma, \; t) = \frac{Q_0}{\gamma^2} \int_{\gamma_{i,\min}}^{\gamma_{i,\max}} d\gamma_i \left(\frac{t_i}{t} \right)^m \frac{\gamma_i^{-q}}{m/\gamma_i t_i + \beta/t_i^{4a} + \delta/t_i^2 + f_*(0)}. \tag{A5}$$

REFERENCES

Aharonian, F. A., et al. 2005, Science, 309, 746
Atoyan, A. M., & Aharonian, F. A. 1997, ApJ, 490, L149
———. 1999, MNRAS, 302, 253
Bednarek, W. 2000, A&A, 362, 646
Belloni, T., Homan, J., Casella, P., van der Klis, M., Nespoli, E., Lewin, W. H. G., Miller, J. M., & Méndez, M. 2005, A&A, 440, 207
Belloni, T., Migliari, S., & Fender, R. P. 2000, A&A, 358, L29
Beloborodov, A. M. 1999, ApJ, 510, L123
Bisnovatyi-Kogan, G. X., & Blinnikov, S. I. 1977, A&A, 59, 111
Bosch-Ramon, V., Aharonian, F., & Paredes, J. M. 2005a, A&A, 432, 609
Bosch-Ramon, V., Romero, G. E., & Paredes, J. M. 2005b, A&A, 429, 267
Böttcher, M. 2001, ApJ, 553, 960
———. 2002, in Proc. The Gamma-Ray Universe, XXII Moriond Astrophysics Meeting, ed. A. Goldwurm, D. N. Neuman, & J. T. T. Van (Hanoi: Gioi), 151
Böttcher, M., & Chiang, J. 2002, ApJ, 581, 127
Böttcher, M., & Dermer, C. D. 2005, ApJ, 634, L81
Böttcher, M., & Liang, E. P. 1998, ApJ, 506, 281
Chen, X., Abramowicz, M. A., Lasota, J.-P., Narayan, R., & Yi, I. 1995, ApJ, 443, L61
Corbel, S., Fender, R. P., Tzioumis, A. K., Nowak, M., McIntyre, V., Durouchoux, P., & Sood, R. 2000, A&A, 359, 251
Corbel, S., Fender, R. P., Tzioumis, T., Tomsick, J. A., Orosz, J. A., Miller, J. M., Wijnands, R., & Kaaret, P. 2002, Science, 298, 196
Corbel, S., et al. 2001, ApJ, 554, 43
Dermer, C. D. 1995, ApJ, 446, L63
Dermer, C. D., & Böttcher, M. 2006, ApJ, 643, 1081
Dermer, C. D., Sturner, S. J., & Schlickeiser, R. 1997, ApJS, 109, 103
Dhawan, V., Mirabel, I. F., & Rodriguez, L. F. 2000, ApJ, 543, 373
Fabbiano, G., Zezas, A., & Murray, S. S. 2001, ApJ, 554, 1035
Fender, R. P., Belloni, T. M., & Gallo, E. 2004, MNRAS, 355, 1105
Fender, R. P., Garrington, S. T., McKay, D. J., Muxlow, T. W. B., Pooley, G. G., Spencer, R. E., Stirling, A. M., & Waltman, E. B. 1999, MNRAS, 304, 865
Fender, R. P., Pooley, G. G., Durouchoux, P., Tilanus, R. P. J., & Brocksopp, C. 2000, MNRAS, 312, 853
Georganopoulos, M., Aharonian, F. A., & Kirk, J. G. 2002, A&A, 388, L25
Giannios, D. 2005, A&A, 437, 1007
Giannios, D., Kylafis, N. D., & Psaltis, D. 2004, A&A, 425, 163
Gregory, P. C., & Taylor, A. R. 1978, Nature, 272, 704
Greiner, J., Cuby, J. G., & McCaughrean, M. J. 2001, Nature, 414, 522
Harlaftis, E. T., & Greiner, J. 2004, A&A, 414, L13
Hua, X.-M., Kazanas, D., & Cui, W. 1998, in AIP Conf. Proc. 431, Accretion Processes in Astrophysics Systems, ed. S. S. Holt & T. R. Kallman (Woodbury: AIP), 108

Hua, X.-M., Kazanas, D., & Titarchuk, L. 1997, ApJ, 482, L57
Kaaret, P., Ward, M. J., & Zezas, A. 2004, MNRAS, 351, L83
Kataoka, J., Takahashi, T., Makino, F., Inoue, S., Madejski, G. M., Tashiro, M., Urry, C. M., & Kubo, H. 2000, ApJ, 528, 243
Kazanas, D., Hua, X.-M., & Titarchuk, L. 1997, ApJ, 480, 735
Kniffen, D. A., et al. 1997, ApJ, 486, 126
Körding, E., & Falcke, H. 2004, A&A, 414, 795
Liang, E. P. 1998, Phys. Rep., 302, 67
Liang, E. P., & Price, R. H. 1977, ApJ, 218, 247
Makishima, K., et al. 2000, ApJ, 535, 632
Markoff, S., Falcke, H., & Fender, R. 2001, A&A, 372, L25
Markoff, S., & Nowak, M. A. 2004, ApJ, 609, 972
Markoff, S., Nowak, M., Corbel, S., Fender, R., & Falcke, H. 2003a, A&A, 397, 645
———. 2003b, NewA Rev., 47, 491
Markoff, S., Nowak, M. A., & Wilms, J. 2005, ApJ, 635, 1203
McClintock, J. E., & Remillard, R. A. 2006, in Compact Stellar X-Ray Sources, ed. W. H. G. Lewin & M. van der Klis (Cambridge: Cambridge Univ. Press), chap. 4
Miller, J. M., et al. 2003, ApJ, 585, L37
Mirabel, I. F., & Rodríguez, L. F. 1994, Nature, 371, 46
Moskalenko, I. V., & Karakula, S. 1994, ApJS, 92, 567
Moskalenko, I. V., Karakula, S., & Tkaczyk, W. 1993, MNRAS, 260, 681
Narayan, R., & Yi, I. 1994, ApJ, 428, L13
Pakull, M. W., & Mirioni, L. 2003, Rev. Mex. AA, 15, 197
Paredes, J. M., Martí, J., Ribó, M., & Massi, M. 2000, Science, 288, 2340
Reig, P., Kylafis, N. D., & Giannios, D. 2003, A&A, 403, L15
Rodriguez, J., Corbel, S., & Tomsick, J. A. 2003, ApJ, 595, 1032
Romero, G. E., Christiansen, H. R., & Orellana, M. 2005, ApJ, 632, 1093
Romero, G. E., Torres, D. F., Kaufman Bernadó, M. M., & Mirabel, I. F. 2003, A&A, 410, L1
Shakura, N. I., & Sunyaev, R. A. 1973, A&A, 24, 337
Shapiro, S., Lightman, A. P., & Eardley, D. M. 1976, ApJ, 204, 187
Sunyaev, R. A., & Titarchuk, L. 1980, A&A, 86, 121
Takahashi, T., et al. 1996, ApJ, 470, L89
Tavecchio, F., Maraschi, L., & Ghisellini, G. 1998, ApJ, 509, 608
Taylor, A. R., Kenny, H. T., Spencer, R. E., & Tzioumis, A. 1992, ApJ, 395, 268
Titarchuk, L. 1994, ApJ, 434, 570
Tomsick, J. A., Corbel, S., Fender, R. P., Miller, J. M., Orosz, J. A., Tzioumis, T., Wijnands, R., & Kaaret, P. 2003, ApJ, 582, 933
Yuan, F., Cui, W., & Narayan, R. 2005, ApJ, 620, 905